

Mobile Small Polarons Explain Conductivity in Lithium Titanium Oxide Battery Electrodes

Matthias Kick,[†] Cristina Grosu,^{†,‡} Markus Schuderer,[†] Christoph Scheurer,[†] and
Harald Oberhofer^{*,†}

[†]*Chair for Theoretical Chemistry and Catalysis Research Center, Technical University of
Munich, Lichtenbergstr. 4, 85747 Garching, Germany*

[‡]*Institute of Energy and Climate Research (IEK-9), Forschungszentrum Jülich, 52425
Jülich, Germany*

E-mail: harald.oberhofer@tum.de

Abstract

Lithium titanium oxide $\text{Li}_4\text{Ti}_5\text{O}_{12}$ (LTO) is an intriguing anode material promising particularly long lived batteries, due to its remarkable phase stability during (dis)charging of the cell. However, its usage is limited by its low intrinsic electronic conductivity. Introducing oxygen vacancies can be one method to overcome this drawback, possibly by altering the charge carrier transport mechanism. We use Hubbard corrected density-functional theory (DFT+U) to show that polaronic states in combination with a possible hopping mechanism can play a crucial role in the experimentally observed increase of electronic conductivity. To gauge polaronic charge mobility, we compute relative stabilities of different localization patterns and estimate polaron hopping barrier heights. With this we finally show how defect engineering can indeed raise the electronic conductivity of LTO up to the level of its ionic conductivity, thereby explaining first experimental results for reduced LTO.

Introduction

Energy storage solutions such as Li-ion batteries (LIB) are a key technology in the transition from a fossil fuel based economy to a society based on sustainable resource management.^{1,2} Despite the tremendous advancements in battery research over the last few years,³ durability and especially storage capacity still need significant improvements for batteries to represent a viable alternative e.g. in the transport and mobility sectors.^{2,4} One promising material envisioned as a potential remedy for these problems in conventional as well as all-solid state batteries (ASSB) is lithium titanium oxide (LTO).² Zero strain insertion, high cycling stability and a stable charge/discharge plateau render LTO an excellent anode material for long living batteries.^{2,4-6} Its general use, however, is still limited by the fact that LTO suffers from a very low intrinsic electronic conductivity.^{7,8} One way to overcome this drawback is to expose LTO to a reductive hydrogen atmosphere at elevated temperatures, leading to the formation of oxygen vacancies. As experimental data shows,⁹ this not only causes a color change from white to blue but also lowers electronic resistance and impedance. Moreover, this blue LTO also shows improved Li-ion mobility compared to pristine white LTO.⁹

Unfortunately, neither of these improvements in carrier mobility are currently fully understood from a mechanistic viewpoint. Yet, first hints at the nature of the improved electronic conductivity in LTO emerged recently with the experimental discovery of paramagnetic Ti^{3+} centers.⁸⁻¹¹ The significance of these becomes apparent considering an analogous case in TiO_2 , where oxygen vacancies are known to lead to the formation of small polarons mainly localized on Ti sites.¹²⁻¹⁴ While these polarons are somewhat attracted to the vacancy itself,^{15,16} they were also shown to be very mobile, with kinetic barriers that can easily be overcome at room temperature.¹⁷ In this context we studied the formation and stability of polarons in bulk LTO, as well as the kinetic barriers separating them. Especially the latter strongly hints at a polaron hopping mechanism as the source of the observed improvement of electronic conductivity in blue LTO.

Results

For our analysis we considered a $2 \times 2 \times 1$ supercell of $\text{Li}_4\text{Ti}_5\text{O}_{12}$ (LTO) in its most stable⁶ spinel configuration,¹⁸ and created an oxygen vacancy at the energetically most favorable of the symmetry inequivalent sites (cf. supplementary material). This realization of the structural Li/Ti disorder is known to exhibit a Ti-deficient zone separating titanium layers as illustrated in Figure 1. It therefore lets us examine the interplay between structure, in the form of Li-rich and Li-poor regions, and function of the material. Removing a neutral oxygen atom from the simulation cell gives rise to two excess electrons, which can form two polaronic Ti^{3+} centers. In standard semi-local LDA¹⁹ or GGA²⁰ based DFT these can generally not be described at all due to the functionals’ well known charge and spin delocalization errors.²¹ As a cost-efficient remedy, we here make use of the popular Hubbard corrected^{22–24} variant of the PBE²⁰ functional (PBE+U) in combination with the matrix control approach.^{25,26} This combination has not only been shown to yield easy access to all manners of polaron configurations but also to yield excellent results compared to the computationally much more expensive hybrid DFT functionals.¹⁵ Given the great structural complexity of defect-rich LTO, there is a large number— $\binom{40}{2} = 780$ —of unique polaron localization patterns even in our relatively small simulation box. To distinguish them we calculated their relative stability according to $E_{\text{rel}} = E_{\text{tot},i} - E_{\text{tot},\text{min}}$, where $E_{\text{tot},i}$ denotes the total energy of a given simulation box calculated with DFT and $E_{\text{tot},\text{min}}$ denotes the total energy of the most stable structure found so far. Hence, following standard procedures,¹² the most stable configuration serves as zero point of our energy scale, with all other configurations possessing positive relative energy.

An exhaustive computational sampling is complicated further by the fact that the electrons can localize both in a triplet or an open-shell singlet configuration.^{12,13} On the other hand, many of these patterns are, if not fully degenerate, at least very close in energy. For a first demonstration of the existence and mobility of polarons in LTO and their influence on the electronic conductivity a complete sampling of all configurations is therefore not nec-

essary. Instead, we focus on triplet configurations and localization patterns representative for the system as a whole. In detail, we considered 13 patterns with different distances to the defect site, localized within different Ti layers in the bulk unit cell. To distinguish them, we adapt a naming convention used in our earlier work¹⁵ to the case of LTO, cf. Figure 1. We found the most stable defect position to be located in the center of the Ti-rich region of our layered LTO model (black circle in Figure 1, cf. also supplementary material). This localization is not at all surprising, as it allows the O-vacancy to be as far as possible from the Li-rich zone of our simulation cell and the structural distortions caused by it. Using this defect position throughout, Table 1 lists our obtained results regarding the relative stability of different polaron localization patterns. We found that the most stable

Table 1: Relative stabilities of the most representative polaronic configurations. The systems are ordered by their relative stabilities. A complete list of calculated systems can be found in the supplementary information. Also shown is the shortest periodic distance between the two Ti^{3+} centers ($d_{\text{Ti}^{3+}-\text{Ti}^{3+}}$).

For vertical layer-layer distances see Fig. 1.					
system	E_{rel} [eV]	$d_{\text{Ti}^{3+}-\text{Ti}^{3+}}$ [Å]	system	E_{rel} [eV]	$d_{\text{Ti}^{3+}-\text{Ti}^{3+}}$ [Å]
L3-7/L2-9	0.00	6.6	L5-1/L3-12	0.45	7.9
L3-8/L3-4	0.12	6.0	L4-2/L4-4	0.75	5.9
L3-7/L3-12	0.13	7.9	L1-1/L1-4	0.77	10.0
L2-7/L2-8	0.14	5.9	L5-5/L4-2	0.82	7.9
L3-9/L3-12	0.23	3.0	L4-3/L4-4	1.00	6.0
L2-9/L2-12	0.26	2.9	L5-1/L5-5	2.59	6.0

configurations are those where one polaron is located in L2 and the other is located in L3 (cf. Figure 2a), followed by configurations where both polarons are either located in L2 or L3. The main difference is that “same-plane” polarons approach each other more closely and hence Coulomb repulsion is more pronounced compared to the most stable L3-X/L2-Y configurations. Furthermore, our analysis shows that there is also a tendency for polarons to be less stable the closer they are located to the defect site. This is clearly indicated by the configurations where both excess electrons are localized on Ti atoms belonging to layers L4 or L5 (see supplementary information for detailed distances to the defect site). Both of

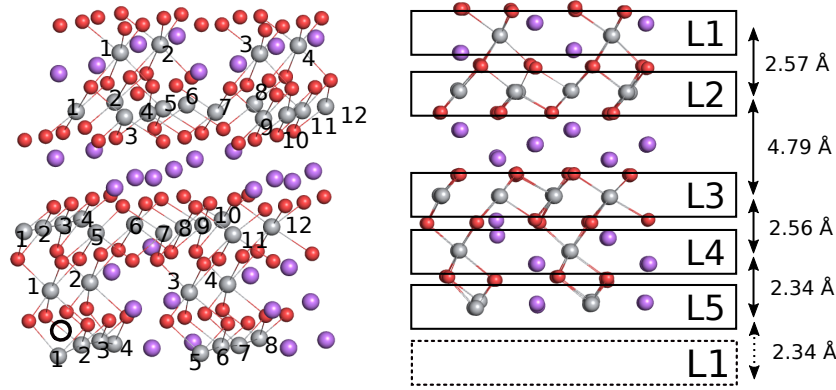


Figure 1: Sketch of the site naming convention of the different localization patterns. $Lx-m/Ly-n$ specifies the localization of one electron within layer Lx on atom m with the second electron localized in layer Ly on atom n . Additionally, the position of the oxygen vacancies is marked with a black circle. Titanium atoms are depicted as grey spheres, oxygen atoms are shown as red spheres. On the right, arrows and numbers indicate the average inter layer titanium distance within the given unit cell.

these effects compete with each other, such that polarons try to adopt configurations with maximal distances to the defect and between each other. This situation seems similar to TiO_2 where the oxygen defect is acting as a charge trapping center.^{27,28} However, in LTO one can not directly extract a clear stability trend with the distance to the defect, as positively charged Li-ions also show some influence on the overall stabilities of the polarons.²⁹ Indeed, our choice of LTO cell allows us to quantify their influence, considering the fact that all our most stable defect configurations are located next to the Li-rich zone situated between L2 and L3.

Finally, in order to gauge the polaron mobility we calculate hopping barriers between our most stable configuration and adjacent Ti atoms. To this end, we again make use of the matrix control approach,^{25,26} but with a modified occupation matrix scheme outlined in the supplementary material. This approach allows us to restrain the electronic configuration of the system along a pre-selected reaction coordinate x , which linearly interpolates between two stable polaronic states, localized at neighboring atoms. Representatively for all hopping processes in the system we compute the “in-plane” transition of L3-7/L2-10 ($x = 0.0$) to L3-7/L2-9 ($x = 1.0$) and the “out-of-plane” transition of L3-7/L1-3 ($x = 0.0$) to L3-7/L2-9

($x = 1.0$).

We illustrate this pathway in Figure 2, which in a) shows the spin density of the final state L3-7/L2-9 and in b) depicts the relaxation of atoms from their respective sites in the pristine crystal for the transition from L3-7/L2-10 to L3-7/L2-9 via a transition state. We thereby only depict O atoms nearest to the involved Ti sites as only these show any significant distortion during a full geometry optimization. Figure 2b clearly shows relaxation of the O-atoms towards the respective Ti^{3+} sites in the initial (L2-10, blue) and final (L2-9, red) states, indicating a small polaron hopping mechanism. A similar picture arises for the transition from L3-7/L1-3 to L3-7/L2-9 (not pictured).

The energy profiles of these two transitions are depicted in Figure 3. As highlighted by the dashed black lines, the hopping barriers for transition L3-7/L2-10 to L3-7/L2-9 and for transition L3-7/L1-3 to L3-7/L2-9 are 186 meV and 583 meV respectively, with the later being much larger due to the already significant energy difference of 485 meV between the two stable states. With these barrier heights we can roughly estimate the in- and out-of-plane conductivity based on a simple hopping model (cf. supplementary material) and using an experimentally measured density of Ti^{3+} centers of 13.1 at%³⁰ as a measure for the charge carrier density. For the in-plane conductivity we thus find a value of 95.3 mS/cm, while the significantly higher out-of-plane hopping barrier results in a much smaller conductivity of 17×10^{-6} mS/cm. To put these results into context, even our lower bound for the conductivity of reduced LTO is already five orders of magnitude higher than the pristine material,³⁰ while our ideal upper bound is of the order of the ion conductivities in currently employed electrolytes.³¹ Note that the estimate for the ideal conductivity rests on the assumption that there are no other, significantly higher barriers along the whole pathway of charge percolation through the crystal. This implies a distribution of defects aligned along the [100] axis of the crystal. Considering the fairly high density of oxygen defects present in blue LTO, such a case is certainly achievable.

Discussion

To conclude, our stability analysis clearly indicates that the experimentally observed Ti^{3+} centers in reduced LTO can in fact be the result of small polaron formation. Moreover, comparatively small barrier heights indicate that charge hopping dynamics can already occur at room temperature. This renders a polaron hopping mechanism to be the most likely origin of the increased electronic conductivity observed in blue LTO. Indeed a simple conductivity model puts even the worst estimate of 17×10^{-6} mS/cm five orders of magnitude above pristine LTO. On the other hand, the ideal predicted case based on an in-plane hopping mechanism would lead to a conductivity of 100 mS/cm, which, though significantly lower than that of other anode materials,^{31–33} is nevertheless comparable to the ion conductivities of the pristine material and super-ionic conductors.^{2,10,34} Moreover, the existence of polarons also hints at a mechanism for the improved ion diffusivity in blue LTO, which is about twice that of pristine LTO.³⁰ The presence of polarons, which we have shown to localize near Li-rich regions, could serve to “soften” the environment for Li-diffusion by screening the positive charge carriers. Thus, both, the ideal polaron conductivity of blue LTO, and its improved Li diffusivity, would make it a suitable option for an anode material for use in tomorrow’s batteries. Note that our results show a very wide range of potential conductivity values, depending on defect patterning, local crystal structure and crystal orientation. Our study thus highlights the potential and also pitfalls of defect engineering as a means for the generation of mobile charge carriers in otherwise insulating materials.

Methods

All necessary calculations have been carried out using the FHI-aims code.³⁵ To achieve adequate electron localization we used the DFT+U²³ variant of the PBE²⁰ exchange correlation functional. In detail we used the rotationally invariant +U form²⁴ with the double-counting correction in the fully localized limit.³⁶ The Ti 3*d* atomic like basis functions served as Hub-

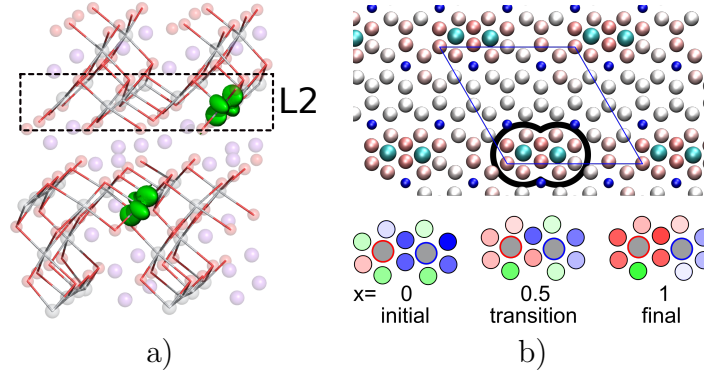


Figure 2: a) Spin density of the most stable configuration L3-7/L2-9 of our simulation. Isosurface level $0.015 \text{ e}\text{\AA}^{-3}$. b) Top: cut through the simulation cell showing the L2-layer, showing the distortion of the lattice at the transition state. Atoms in cyan indicating the L2-9 and L2-10 positions respectively. Darker red colors indicate a stronger movement during the transition from L3-7/L2-10 to L3-7/L2-9. Note that only nearest neighbor oxygen atoms show significant movement, indicating indeed the hopping of a small polaron. Bottom: schematic of the movement of oxygen atoms from their undistorted sites for the transition from L3-7/L2-10 (left) to L3-7/L2-9 (right) via a transition state (center). Circles filled in red hues indicate a predominant movement of the respective O atom towards the Ti atom at L2-9 (red circle filled with grey), while blue hues depict a movement towards L2-10 (blue circle filled with grey). Circles filled in green hues show movement not clearly aimed at either Ti atoms. In all cases darker colors indicate stronger movement.

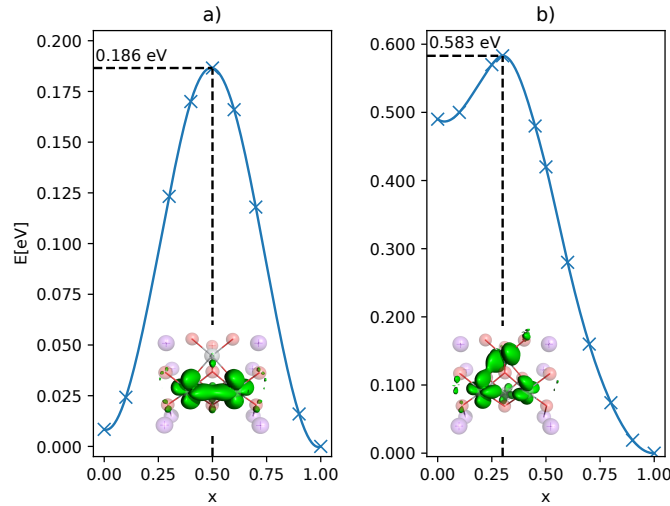


Figure 3: Calculated barrier profiles for the transition L3-7/L2-10 to L3-7/L2-9 (a) and L3-7/L1-3 to L3-7/L2-9 (b). In both plots $x = 1.0$ is equal to configuration L3-7/L2-9. The lowest lying configuration in energy serves as zero point for the energy scale. Also shown is the spin density of the corresponding transition state. Isosurface level $0.015 \text{ e}\text{\AA}^{-3}$.

bard projectors and a U value of 2.65 eV has been applied. Numerical convergence has been reached using a *tight tier1* basis—roughly equivalent to a polarized triple zeta split valence Gaussian type orbital basis set³⁷—employing a $2 \times 2 \times 1$ k-point grid. Geometries have been relaxed until residual force fell below 10^{-2} eV/Å. A detailed description of the methodology used to estimate barriers is given in the supplementary material.

Acknowledgements

The authors would like to thank the German Research Foundation DFG (Grant OB425/4-1) and the Solar Technologies Go Hybrid Initiative of the State of Bavaria for support. Partially funded by the Deutsche Forschungsgemeinschaft (DFG, German Research Foundation) under Germany’s Excellence Strategy EXC 2089/1 390776260.

References

- (1) Islam, M. S.; Fisher, C. A. J. Lithium and sodium battery cathode materials: computational insights into voltage, diffusion and nanostructural properties. *Chem. Soc. Rev.* **2014**, *43*, 185–204.
- (2) Zhao, B.; Ran, R.; Liu, M.; Shao, Z. A comprehensive review of $\text{Li}_4\text{Ti}_5\text{O}_{12}$ -based electrodes for lithium-ion batteries: The latest advancements and future perspectives. *Mater. Sci. Eng. R Rep* **2015**, *98*, 1–71.
- (3) Chu, S.; Majumdar, A. Opportunities and challenges for a sustainable energy future. *Nature* **2012**, *488*, 294 EP–.
- (4) Armand, M.; Tarascon, J.-M. Building better batteries. *Nature* **2008**, *451*, 652 EP–.
- (5) Aricò, A. S.; Bruce, P.; Scrosati, B.; Tarascon, J.-M.; van Schalkwijk, W. Nanostruc-

- tured materials for advanced energy conversion and storage devices. *Nat. Mater.* **2005**, *4*, 366–377.
- (6) Heenen, H. H.; Scheurer, C.; Reuter, K. Implications of occupational Disorder on ion mobility in $\text{Li}_4\text{Ti}_5\text{O}_{12}$ battery materials. *Nano Lett.* **2017**, *17*, 3884–3888.
 - (7) Yuan, T.; Yu, X.; Cai, R.; Zhou, Y.; Shao, Z. Synthesis of pristine and carbon-coated $\text{Li}_4\text{Ti}_5\text{O}_{12}$ and their low-temperature electrochemical performance. *J. Power Sources* **2010**, *195*, 4997–5004.
 - (8) Yan, B.; Li, M.; Li, X.; Bai, Z.; Yang, J.; Xiong, D.; Li, D. Novel understanding of carbothermal reduction enhancing electronic and ionic conductivity of $\text{Li}_4\text{Ti}_5\text{O}_{12}$ anode. *J. Mater. Chem. A* **2015**, *3*, 11773–11781.
 - (9) Qiu, J.; Lai, C.; Gray, E.; Li, S.; Qiu, S.; Strounina, E.; Sun, C.; Zhao, H.; Zhang, S. Blue hydrogenated lithium titanate as a high-rate anode material for lithium-ion batteries. *J. Mater. Chem. A* **2014**, *2*, 6353–6358.
 - (10) Kaftelen, H.; Tuncer, M.; Tu, S.; Repp, S.; Göçmez, H.; Thomann, R.; Weber, S.; Erdem, E. Mn-substituted spinel $\text{Li}_4\text{Ti}_5\text{O}_{12}$ materials studied by multifrequency EPR spectroscopy. *J. Mater. Chem. A* **2013**, *1*, 9973–9982.
 - (11) Jakes, P.; Granwehr, J.; Kungl, H.; Rüdiger-A, E. Mixed ionic-electronic conducting $\text{Li}_4\text{Ti}_5\text{O}_{12}$ as anode material for lithium ion batteries with enhanced rate capability - impact of oxygen non-stoichiometry and aliovalent Mg^{2+} -doping studied by electron paramagnetic resonance. *Z. Phys. Chem.* **2015**, *229*, 1439–1450.
 - (12) Deskins, N. A.; Rousseau, R.; Dupuis, M. Distribution of Ti^{3+} surface sites in reduced TiO_2 . *J. Phys. Chem. C* **2011**, *115*, 7562–7572.
 - (13) Shibuya, T.; Yasuoka, K.; Mirbt, S.; Sanyal, B. A systematic study of polarons due

- to oxygen vacancy formation at the rutile $\text{TiO}_2(110)$ surface by GGA+U and HSE06 methods. *J. Phys. Condens. Matter* **2012**, *24*, 435504.
- (14) Setvin, M.; Franchini, C.; Hao, X.; Schmid, M.; Janotti, A.; Kaltak, M.; Van de Walle, C. G.; Kresse, G.; Diebold, U. Direct view at excess electrons in TiO_2 rutile and anatase. *Phys. Rev. Lett.* **2014**, *113*, 086402.
- (15) Kick, M.; Reuter, K.; Oberhofer, H. Intricacies of DFT+U, not only in a numeric atom centered orbital framework. *J. Chem. Theor. Comput.* **2019**, *15*, 1705–1718.
- (16) Reticcioli, M.; Setvin, M.; Schmid, M.; Diebold, U.; Franchini, C. Formation and dynamics of small polarons on the rutile $\text{TiO}_2(110)$ surface. *Phys. Rev. B* **2018**, *98*, 045306.
- (17) Kowalski, P. M.; Camellone, M. F.; Nair, N. N.; Meyer, B.; Marx, D. Charge localization dynamics induced by oxygen vacancies on the $\text{TiO}_2(110)$ surface. *Phys. Rev. Lett.* **2010**, *105*, 146405.
- (18) Deschanvres, A.; Raveau, B.; Sekkal, Z. Mise en evidence et etude cristallographique d’une nouvelle solution solide de type spinelle $\text{Li}_1 + x\text{Ti}_2 - x\text{O}_4$ $0 \leq x \leq 0.333$. *Mater. Res. Bull.* **1971**, *6*, 699–704.
- (19) Hohenberg, P.; Kohn, W. Inhomogeneous electron gas. *Phys. Rev.* **1964**, *136*, B864–B871.
- (20) Perdew, J. P.; Burke, K.; Ernzerhof, M. Generalized gradient approximation made simple. *Phys. Rev. Lett.* **1996**, *77*, 3865–3868.
- (21) Cohen, A. J.; Mori-Sánchez, P.; Yang, W. Insights into current limitations of density functional theory. *Science* **2008**, *321*, 792–794.
- (22) Hubbard, J. Electron correlations in narrow energy bands. *Proc. R. Soc. A* **1963**, *276*, 238–257.

- (23) Anisimov, V.; Zaanen, J.; Andersen, O. K. Band theory and Mott insulators: Hubbard U instead of Stoner I . *Phys. Rev. B* **1991**, *44*, 943–954.
- (24) Dudarev, S. L.; Botton, G. A.; Savrasov, S. Y.; Humphreys, C. J.; Sutton, A. P. Electron-energy-loss spectra and the structural stability of nickel oxide: An LSDA+ U study. *Phys. Rev. B* **1998**, *57*, 1505–1509.
- (25) Dorado, B.; Amadon, B.; Freyss, M.; Bertolus, M. DFT + U . *Phys. Rev. B* **2009**, *79*, 235125.
- (26) Allen, J. P.; Watson, G. W. Occupation matrix control of d- and f-electron localisations using DFT + U . *Phys. Chem. Chem. Phys.* **2014**, *16*, 21016–21031.
- (27) Kohtani, S.; Kawashima, A.; Miyabe, H. Reactivity of trapped and accumulated electrons in titanium dioxide photocatalysis. *Catalysts* **2017**, *7*, 303.
- (28) Diebold, U. The surface science of titanium dioxide. *Surf. Sci. Rep.* **2003**, *48*, 53–229.
- (29) Morgan, B. J.; Watson, G. W. GGA+ U description of lithium intercalation into anatase TiO_2 . *Phys. Rev. B* **2010**, *82*, 144119.
- (30) Nasara, R. N.; Tsai, P.-C.; Lin, S.-K. One-step synthesis of highly oxygen-deficient lithium titanate oxide with conformal amorphous carbon coating as anode material for lithium ion batteries. *Adv. Mater. Interfaces* **2017**, *4*.
- (31) Park, M.; Zhang, X.; Chung, M.; Less, G. B.; Sastry, A. M. A review of conduction phenomena in Li-ion batteries. *J. Power Sources* **2010**, *195*, 7904–7929.
- (32) Dutta, A. K. Electrical Conductivity of Single Crystals of Graphite. *Phys. Rev.* **1953**, *90*, 187–192.
- (33) Creffield, G. K.; Down, M. G.; Pulham, R. J. Electrical resistivity of liquid and solid lithium. *J. Chem. Soc., Dalton Trans.* **1974**, 2325–2329.

- (34) Stenina, I. A.; Il'in, A. B.; Yaroslavtsev, A. B. Synthesis and ionic conductivity of $\text{Li}_4\text{Ti}_5\text{O}_{12}$. *Inorg. Mater.* **2015**, *51*, 62–67.
- (35) Blum, V.; Gehrke, R.; Hanke, F.; Havu, P.; Havu, V.; Ren, X.; Reuter, K.; Scheffler, M. Ab initio molecular simulations with numeric atom-centered orbitals. *Comput. Phys. Commun.* **2009**, *180*, 2175–2196.
- (36) Himmetoglu, B.; Floris, A.; de Gironcoli, S.; Cococcioni, M. "Hubbard-corrected DFT energy functionals: The LDA+U description of correlated systems". *Int. J. Quantum Chem.* **2014**, *114*, 14–49.
- (37) Lamiel-Garcia, O.; Ko, K. C.; Lee, J. Y.; Bromley, S. T.; Illas, F. When Anatase nanoparticles become bulklike: Properties of realistic TiO_2 nanoparticles in the 1–6 nm size range from all electron relativistic density functional theory based calculations. *J. Chem. Theor. Comput.* **2017**, *13*, 1785–1793.

Supplementary Information: Mobile Small Polarons Explain Conductivity in Lithium Titanium Oxide Battery Electrodes

Matthias Kick,[†] Cristina Grosu,^{†,‡} Markus Schuderer,[†] Christoph Scheurer,[†] and
Harald Oberhofer^{*,†}

[†]*Chair for Theoretical Chemistry and Catalysis Research Center, Technical University of
Munich, Lichtenbergstr. 4, 85747 Garching, Germany*

[‡]*Institute of Energy and Climate Research (IEK-9), Forschungszentrum Jülich, 52425
Jülich, Germany*

E-mail: harald.oberhofer@tum.de

1 Structures

1.1 Pristine bulk structures

Spinel lithium titanium oxide (LTO, $\text{Li}_4\text{Ti}_8\text{O}_{12}$) crystallizes in the $\text{Fd}\bar{3}\text{m}$ (No. 227) space group. The O atoms form a face center cubic packing (fcc) and occupy the 32e sites within the cubic unit cell. The titanium atoms and one quarter of the lithium atoms are octahedral coordinated by oxygen and occupy the 16d sites. The ratio between Li and Ti atoms at these octahedral sites is $\frac{1}{6}:\frac{5}{6}$. The remaining Li atoms occupy the 8a sites.¹

The mixed occupancy of Ti and Li at the 16d sites can not be realized with the conventional cubic unit cell of $\text{Fd}\bar{3}\text{m}$ as there are only sixteen possible sites resulting in a no integer ratio of Li and Ti atoms if the mixed occupancy would be considered. A suitable

subgroup that allows for the right stoichiometry within a single unit cell is $R\bar{3}m$ (No. 166). The unit cell of this space group is hexagonal. Within this cell the mixed occupancy can be easily realized. It contains 12 sites corresponding to the 16d sites in $Fd\bar{3}m$. Among them one has to distribute two Li atoms and ten Ti atoms to achieve the correct ratio. In total this yields $\binom{12}{2} = 66$ possibilities. Among these one can identify 6 unique structures the others are equivalent by symmetry. All of those are different in energy and are denoted c0001 to c0006. All LTO structure are shown in Figure 1.

These configurations are the starting point for our analysis. We performed pure PBE² calculations. Table 1 list the obtained results. Among all systems, c0002 is identified to be the most stable configuration. Therefore, we continue our analysis using the c0002 structure.

Table 1: Relative stabilities, $E_{\text{rel}}^{\text{LTO}}$, of the different pristine bulk structures. Most stable structure c0002 serves as zero point for the energy scale.

system	$E_{\text{rel}}^{\text{LTO}}[\text{eV}]$
c0001	0.72
c0002	0.00
c0003	2.14
c0004	4.38
c0005	0.77
c0006	0.36

1.1.1 Computational details

Calculations have been performed using the PBE² functional as it is implemented in the CASTEP³ code using a $4 \times 4 \times 2$ k-point grid. Structures have been fully relaxed until forces where below 10^{-2} eV/Å in combination with a plane wave basis set using an energy cut-off of 600 eV.

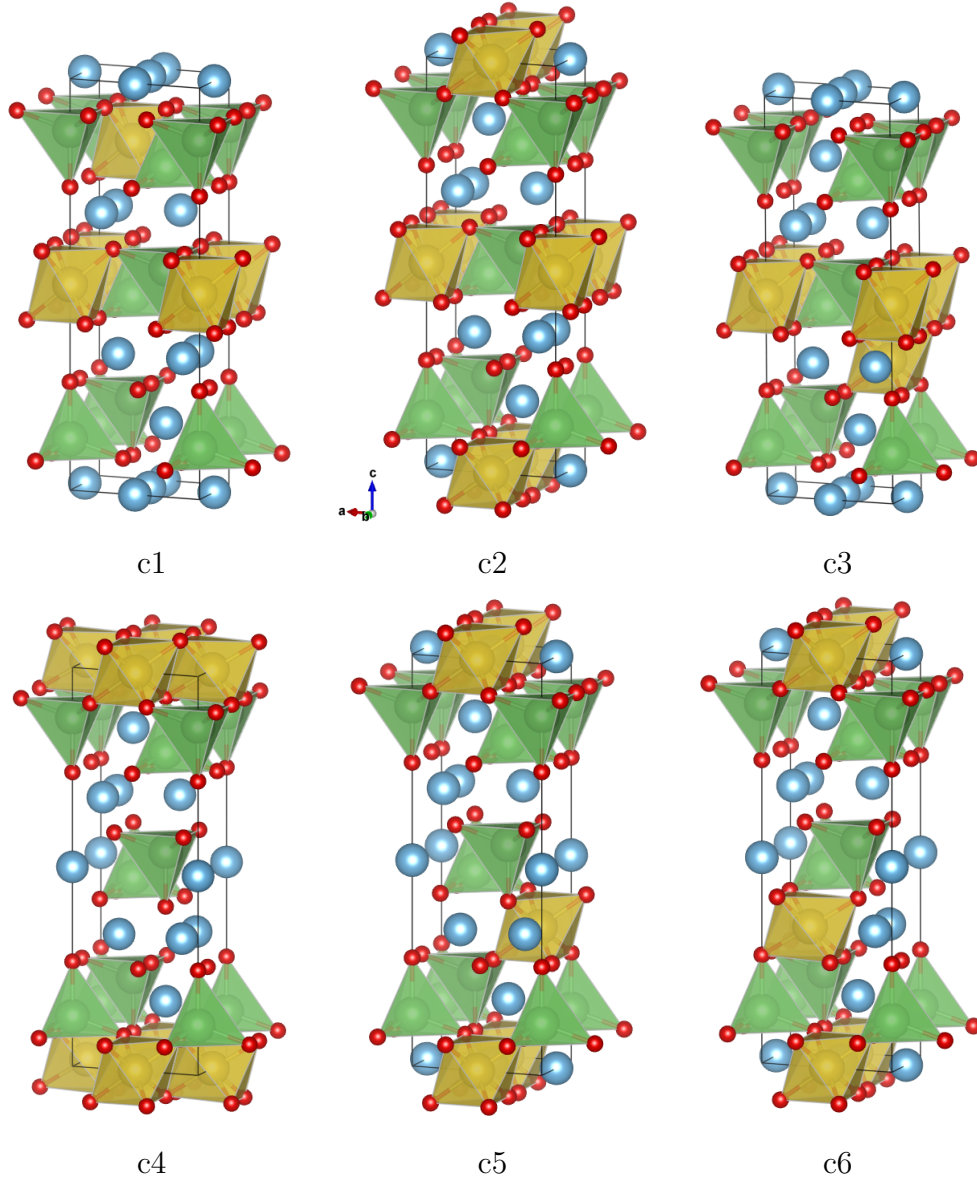


Figure 1: Shown are the different LTO unit cells. Ti atoms are shown in light blue, oxygen atoms are red and Li atoms are shown as green spheres. Tetrahedral and octahedral sites are depicted accordingly.

1.2 Defect bulk structures

Within the c0002 unit cell one can identify nine unique O vacancies all others are equivalent due to symmetry (see Figure 2). For this purpose the Site Occupancy Disorder (SOD) package⁴ has been used.

We embedded each of the nine unique oxygen vacancies into $2 \times 2 \times 1$ supercells, yielding a supercell based on three standard defect free unit cells and one with O vacancy. This structural variety of LTO makes computational sampling rather demanding, therefore, as a first starting point we performed full geometry relaxations using only the PBE functional within FHI-aims. Our results are showed in table 2 where the different structures are named from v1 to v9 according to the position of the oxygen vacancy in the primitive cell. Again, the most stable configuration serves as zero point for the energy scale.

We like to highlight, that in principle one has to consider here all possible configurations of this system to find the true configuration which is lowest in energy. Therefore, this should be seen just as a first attempt to tackle the problem. Considering, neutral, single and doubly charged oxygen defects in combination with all possible localization patterns of polarons is by far not tractable as one has to go beyond LDA or GGA approximations in order to correctly describe the defect states.

Among all nine different vacancy configurations we use the most stable one (v3) as the starting point for all further polaron calculations. The supercell of configuration v3 is shown in Figure 3.

1.2.1 Computational details

All calculations have been performed using the PBE functional as implemented in the FHI-aims code with preoptimized structures obtained from CASTEP calculations. Reciprocal space has been sampled using a $2 \times 2 \times 2$ Monkhorst-Pack⁵ k-point grid. The structures were fully relaxed until forces have been below 10^{-2} eV/Å applying a *light tier1* basis set.

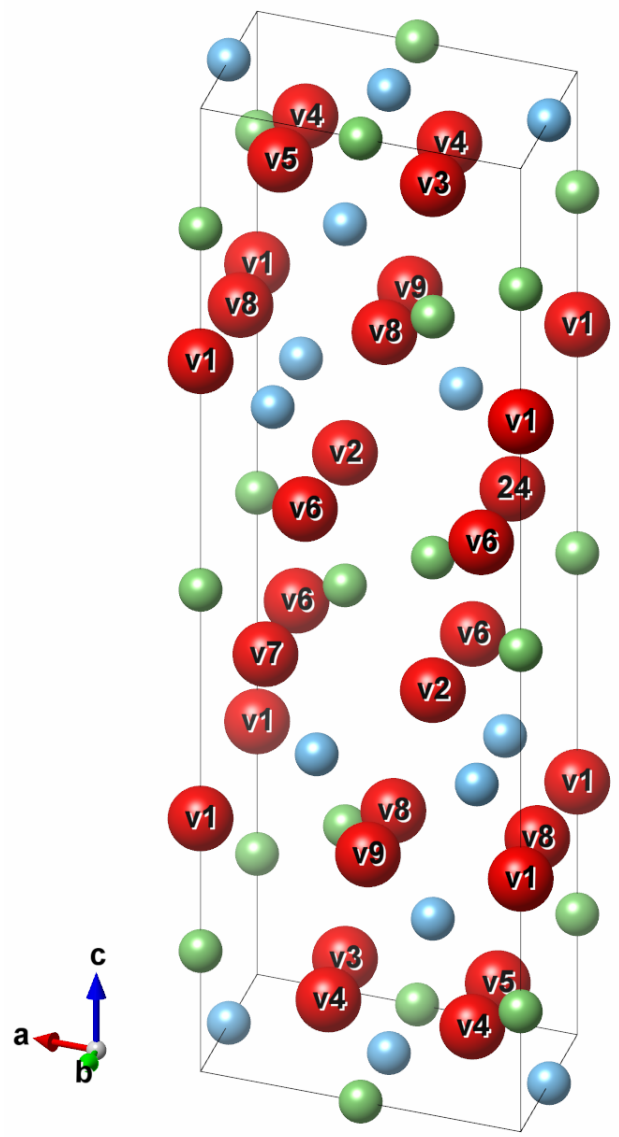


Figure 2: Single unit cell of the c2 LTO structure. Ti atoms are shown in light blue, Li atoms are shown in green and oxygen atoms are displayed as red spheres. The different position for an oxygen vacancy are named from v1 to v9. Double naming indicates a symmetry equivalent site.

Table 2: Relative stabilities, $E_{\text{rel}}^{\text{LTO}+\text{O}_v}$, of the different bulk structures with O vacancy. Most stable structure v3 serves as zero point for the energy scale.

system	$E_{\text{rel}}^{\text{LTO}+\text{O}_v} [\text{eV}]$
v1	1.58
v2	1.95
v3	0.00
v4	0.38
v5	1.06
v6	0.87
v7	1.13
v8	0.78
v9	1.13

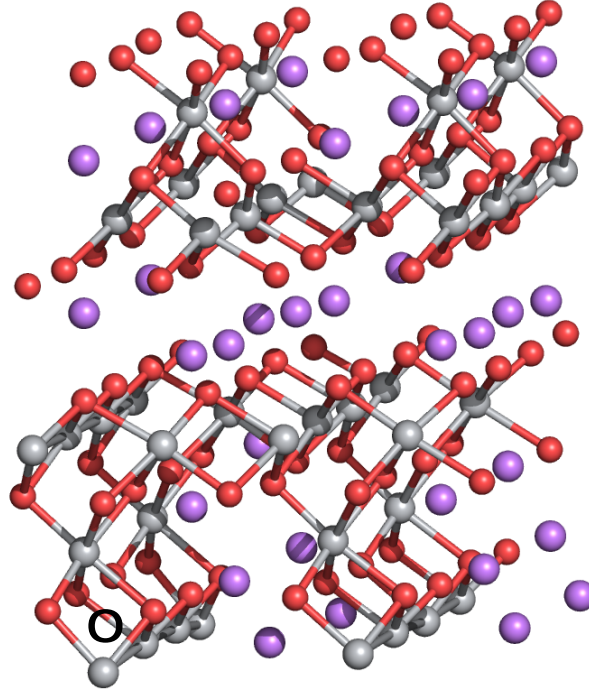


Figure 3: Supercell structure consisting of four LTO c2 cells including the v3 vacancy. The O vacancy is marked with a black circle. Li atoms are purple. O atoms are shown as red spheres. Ti atoms are shown as grey spheres.

2 Polaron calculations

2.1 Localizing the Polarons

From a methodological point of view, a key aspect of DFT+U is the choice of the correct projector-dependent Hubbard U value.^{6,7} A common strategy would be to choose the value according to the experimentally determined defect position within the band gap.^{7,8} However, owing to the relative novelty of blue LTO, there are no such results to be found in the literature. From TiO₂ the gap state position is experimentally known to be about 1 eV below the conduction band minimum (CBM)⁹. Arguably, titanium atoms in both LTO and TiO₂ are embedded in a similar chemical environment, leading to a similar position of the defect state within the band gap. This assumption is further supported by the observation that both defective TiO₂ and LTO show the same blue color.^{10–12} Based on this approximation, all our analysis are conducted with a U value of 2.65 eV, yielding gap states at around 1 eV below the CBM for the most stable polaronic configurations found. For localizing the electrons at different Ti atoms we made use of the matrix control approach^{13,14}. We started with the occupation matrices obtained from a pure PBE² run and used this as input for the matrix control routines. To obtain electron localization in specific orbitals on a specific Ti atoms, we modified the corresponding diagonal matrix element to 1. Afterwards, full geometry optimization is performed by fixing this modified occupation matrix. To obtain full self-consistency, we used the obtained geometry and the wave function information as input for a second run without constraining the occupation matrix. Table 3 contains the complete list of calculated polaron systems and their relative stabilities. The relative stabilities have been calculated according to

$$E_{\text{rel}} = E_{\text{tot},i} - E_{\text{tot, most stable structure}} \quad , \quad (1)$$

where $E_{\text{tot},i}$ is the total energy of a specific configuration and $E_{\text{tot, most stable structure}}$ is the total energy of the most stable configuration. By this, all other less stable configurations show positive energies.⁸

Table 3: Relative stabilities of the calculated polaronic configurations. Here, we only considered triplet configurations. Furthermore, d_{V_O} indicates the distance from the Ti^{3+} center to the next periodic oxygen vacancy in the unit cell. Only the distances within the unrelaxed defect supercell have been considered.

system	E_{rel} [eV]	d_{V_O} [Å]	system	E_{rel} [eV]	d_{V_O} [Å]
L3-7/L2-9	0.00	6.52/7.47	L3-9/L3-12	0.23	5.05/6.55
L3-7/L2-11	0.01	6.52/8.63	L2-8/L2-12	0.23	9.45/7.38
L3-7/L2-10	0.01	6.52/8.50	L2-8/L2-11	0.23	9.45/8.63
L3-7/L2-7	0.02	6.52/7.43	L3-9/L3-10	0.26	5.05/4.92
L2-7/L3-5	0.07	7.43/4.95	L5-1/L3-9	0.43	2.08/5.05
L3-8/L3-4	0.12	6.51/4.93	L5-1/L3-12	0.45	2.08/6.55
L3-11/L3-12	0.12	6.34/6.55	L3-7/L1-3	0.49	6.52/6.69
L3-7/L3-12	0.13	6.52/6.55	L4-2/L4-4	0.75	3.71/3.68
L2-7/L2-8	0.14	7.43/9.45	L4-3/L4-2	0.77	6.99/3.71
L2-7/L2-12	0.15	7.43/7.38	L1-1/L1-4	0.77	6.84/6.70
L3-5/L3-6	0.19	4.95/4.81	L5-5/L4-2	0.82	6.22/3.71
L3-5/L4-2	0.19	4.95/3.71	L4-3/L4-4	1.00	6.99/3.68
L3-7/L3-9	0.20	6.52/5.05	L5-1/L5-5	2.59	2.08/6.22

2.2 Computational details

Electronic structure calculations have been performed entirely using the FHI-aims program package¹⁵. All structure optimizations have been performed with applying the DFT+U^{16–18} variant of the PBE exchange correlation functional using the fully-localized limit (FLL)⁶ as double counting correction. The Ti 3d atomic basis functions serve as Hubbard projectors in each run. Only the on-site representation¹⁹ for the DFT+U occupation matrix have been used in combination with a U value of 2.65 eV. Numerically convergence have been already reached with a *tight tier1* basis set. Reciprocal space has been sampled using a 2 x 2 x

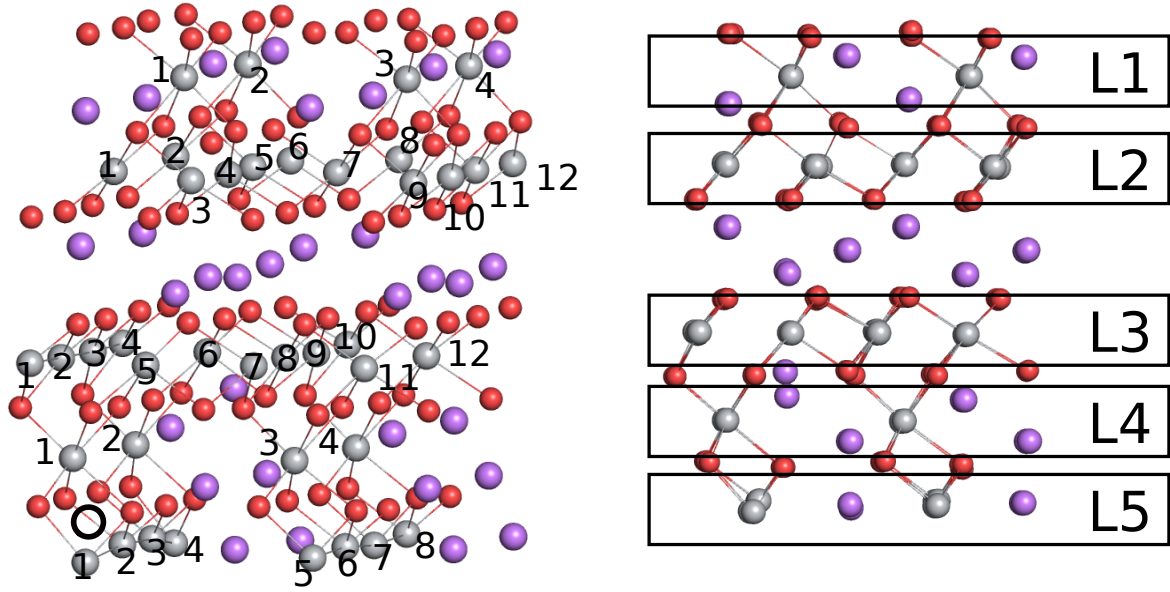


Figure 4: Site naming convention of the different localization patterns. $Lx-m/Ly-n$ thus specifies the localization of one electron within layer Lx on atom m with the second electron localized in layer Ly on atom n . The position of the oxygen vacancy is also marked with a black circle. Titanium atoms are depicted as grey spheres, oxygen atoms are shown as red spheres.

2 Monkhorst-Pack⁵ k-point grid. The structures were fully relaxed until forces have been below 10^{-2} eV/Å.

If not otherwise noted, all structures related to the polaron calculations have been fully optimized with PBE+U(=2.65) only.

3 Barrier calculations

3.1 Obtaining the barrier profile

For the barrier profiles we again make use of the matrix control approach. However, instead of fixing all the occupation matrices we only fix the occupation matrices of the atoms between which we assume electron hopping to occur. In detail we studied the hopping of one electron from L3-7/L2-3 to L3-7/L1-9 and from L3-7/L2-10 to L3-7/L2-9. For this we define a reaction coordinate x which describes the occupation matrices of both atoms between the

hopping process. The occupation matrix \mathbf{n}' for a certain atom A and a certain atom B is then defined according to

$$\mathbf{n}'_A = x\mathbf{n}_A^{\text{Ti}^{3+}} + (1-x)\mathbf{n}_A^{\text{Ti}^{4+}} \quad , \quad (2a)$$

$$\mathbf{n}'_B = (1-x)\mathbf{n}_B^{\text{Ti}^{3+}} + x\mathbf{n}_B^{\text{Ti}^{4+}} \quad . \quad (2b)$$

$\mathbf{n}^{\text{Ti}^{3+}}$ is the occupation matrix where the excess electron is fully localized at a certain atom, this occupation matrix is obtained from a full self-consistent calculation as it is described in section 2.1. $\mathbf{n}^{\text{Ti}^{4+}}$ is the occupation matrix at a certain atom if none of the excess electrons is localized. Going from L3-7/L2-10 to L3-7/L2-9 this means $\mathbf{n}_A^{\text{Ti}^{3+}}$ belongs to the self-consistent occupation matrix of L2-9 in system L3-7/L2-9 and $\mathbf{n}_A^{\text{Ti}^{4+}}$ belongs to the occupation matrix of atom L2-9 in the L3-7/L2-10 system. Occupation matrix $\mathbf{n}_B^{\text{Ti}^{3+}}$ would then be the self-consistent occupation matrix of atom L2-10 in system L3-7/L2-10 and $\mathbf{n}_B^{\text{Ti}^{4+}}$ corresponds to the self-consistent occupation matrix of atom L2-10 in system L3-7/L2-9. As a next step we performed full structure relaxations with applying the above described constraints. This means that our chosen reaction coordinate directly translates also to a structural change along the reaction path. Table 4 lists the obtained energies with respect to the configuration lowest lying in energy. However, this is the energy with applied constraints from the matrix control approach. In addition, in order to further judge the quality of this approach we use the obtained wave-function information from the saddle point and evaluate the DFT+U functional again without constraining the occupation matrices (red points in Figure 5). This gives a direct estimate how the electron density is able to adapt to the applied bias potential. For the transition L3-7/L2-10 to L3-7/L2-9 depicted in Figure 5a both energies agree remarkable well, with a difference of only about 6 meV. For the other transition considered here, L3-7/L1-3 to L3-7/L2-9, (Figure 5b) the difference is with 56 meV significantly larger. To analyse this further, we calculated the difference in the sum of the diagonal elements between applied occupation matrix \mathbf{n}' and the actual occupation matrix

Table 4: Listed are the points calculated for the barrier profile which is shown in figure 5. All points have been calculated from the matrix-control run. The lowest energy configuration serves as zero point for the energy scale. The notation in brackets corresponds to the self-consistent polaron configuration.

x	L3-7/L2-10 \rightarrow L3-7/L2-9 [eV]	L3-7/L2-3 \rightarrow L3-7/L1-9 [eV]
0.00	0.008 (L3-7/L2-10)	0.485 (L3-7/L1-3)
0.10	0.024	0.501
0.25	-	0.565
0.30	0.123	0.583
0.40	0.170	-
0.45	-	0.483
0.50	0.186	0.416
0.60	0.166	0.280
0.70	0.118	0.162
0.80	-	0.074
0.90	0.016	0.019
1.00	0.000 (L3-7/L2-9)	0.000 (L3-7/L2-9)

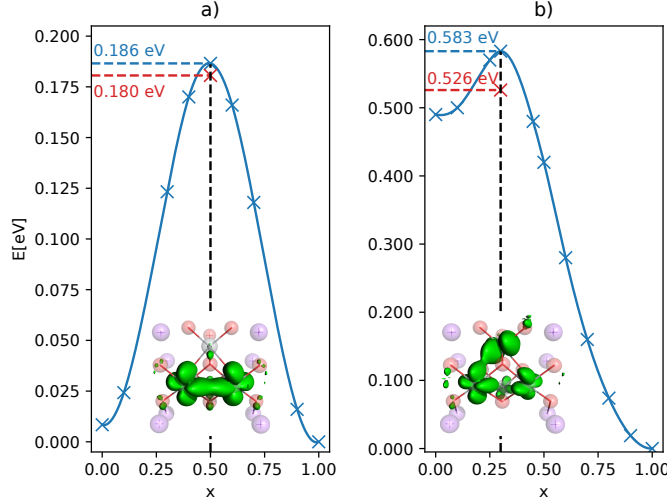


Figure 5: Calculated barrier profile for the transition L3-7/L2-10 to L3-7/L2-9 (a) and L3-7/L1-3 to L3-7/L2-9 (b). $x = 1.0$ is equal to configuration L3-7/L2-9. Blue points are energies obtained with fixed occupation matrix according to eq. 2a in both subfigures. Red points are DFT+U energies calculated from the wave-function obtained from the matrix control run. The lowest lying configuration in energy serves as zero point for the energy scale. Also shown is the spin density of the corresponding transition state. Isosurface level $0.015 \text{ e}\text{\AA}^{-3}$.

\mathbf{n} determined from the wave function at the transition state points, $\Delta = \sum_n |n'_{nn}| - |n_{nn}|$. For transition L3-7/L2-10 to L3-7/L2-9 the highest deviation is for the occupation of L2-9 with a value of 0.036. Contrary, for transition L3-7/L1-3 to L3-7/L2-9 our analysis yields a deviation of 0.176 for the occupation matrix at L2-8. This large difference is due to the electron not only being located at L2-8 and L1-3 but also at neighboring titanium atoms. This might indicate that the applied bias potential does not fit the transition state equally well as in the case of the L3-7/L2-10 to L3-7/L2-9 transition and hence is responsible for the observed difference in barrier height. However, this problem is closely related to the problem of defining proper fragments in CDFT.²⁰ Yet, given the fact that this specific transition already shows a significant energy difference of 485 meV between the two stable states, this discrepancy is most likely of minor importance. Our new approach is thus capable of gauging hopping barriers at nearly no overhead over standard DFT calculations. Our results which we obtain for a U value of 2.65 eV are listed in table 5. It should be highlighted, that

Table 5: Barrier heights calculated from the density obtained from the matrix control run.

x	L3-7/L2-10 \rightarrow L3-7/L2-9	L3-7/L2-3 \rightarrow L3-7/L1-9
	[eV]	[eV]
0.30	-	0.526
0.50	0.180	-

the obtained barriers sensitively depend on the applied U value, however, this is a general aspect of DFT+U and not a result of the here applied strategy for obtaining the barrier profiles. Moreover, hybrid functionals should suffer from this drawback too. The U value in DFT+U determines the strength of the on-site coulomb repulsion and hence it determines the amount of how DFT+U will accounts for the self-interaction error. In hybrid functional the mixing factor determines the amount of exact exchange and hence how much a specific hybrid functional accounts for the self-interaction error.

3.1.1 Marcus reaction coordinate

Going along reaction coordinate x the polaron hopping from atom A to atom B occurs as the system passes the transition state. By again exploiting the matrix control approach one is able to constrain the electron at a certain atom and thus preventing the electron to hop. In figure 6 we are showing the corresponding results. Blue dots have been obtained as described in section 3.1, for orange dots we use the structure obtained for a certain x and use the occupation matrix control to constrain the polaron to one specific site. No geometry relaxation have been allowed during that procedure.

In a next step, this allows to define a new reaction coordinate according to,

$$\Delta E = E(x, A) - E(x, B) \quad . \quad (3)$$

Here, $E(x, A)$ is the energy if the electron is located on atom A. Whereas $E(x, B)$ is the energy if the electron is located at atom B. For both energies the same geometry has been

used. In Figure 7 we show the new reaction profile. Clearly, Figure 7b indicates an early transition state for the hopping from L3-7/L1-3 to L3-7/L2-9.

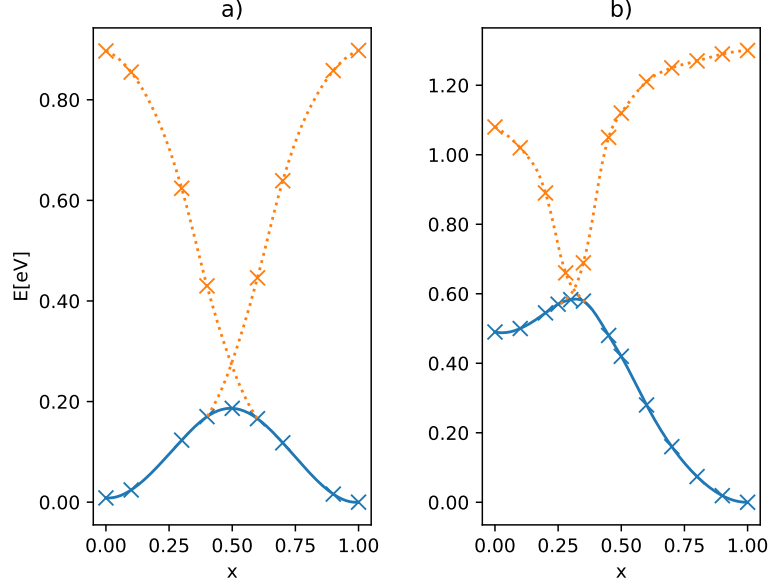


Figure 6: Full reaction profile according to reaction coordinate x which defines the occupation matrices according to eq. 2a and eq. 2b respectively. Blue curve and blue points have been obtained according to the description in section 3.1. L3-7/L2-10 to L3-7/L2-9 is shown in (a) and L3-7/L1-3 to L3-7/L2-9 is depicted in (b). $x = 1.0$ is equal to configuration L3-7/L2-9.

3.2 Computational details

For the barrier calculations we applied the same computational settings as described in section 2.2.

3.3 Conductivity model

Using the barriers ΔE of 186 meV and 583 meV for the in- and out-of-plane polaron transfer, respectively, as representative for the hopping in the LTO crystal, we first compute the respective hopping rates using a simple transition state theory:²¹

$$k_{\text{hop}} = \frac{k_B T}{h} e^{-\Delta E / k_B T} \quad (4)$$

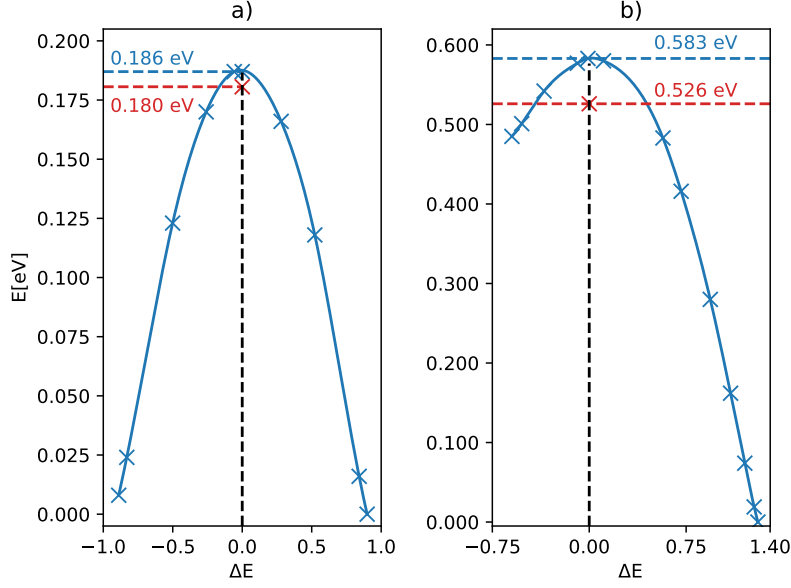


Figure 7

Here, k_B , T , and h denote the Boltzmann constant, the temperature, and Planck's constant, respectively. As a first estimate we here also assume entropic effects to play a minor role for the electronic transition considered here.

These rate constants can then be used in a simple Einstein-Smoluchowsky model of the carrier mobility²¹

$$\mu = \frac{ea^2k_{\text{hop}}}{k_BT}, \quad (5)$$

where e is the elementary charge and a is the distance between the initial and final polaron localization sites. The such calculated mobilities finally allow us to estimate the system's conductivity σ using the number density of charge carriers n and²¹

$$\sigma = en\mu. \quad (6)$$

Thereby, n has been taken from experimental measurements of LTO to be 13.1at% which suggest $2.9 \times 10^{-3} \text{ \AA}^{-3}$ for our simulation cell. Using a temperature of 300 K we arrive at conductivities of $9.53 \times 10^{-02} \text{ S/cm}$ and $1.7 \times 10^{-08} \text{ S/cm}$ for the in- and out-of-plane polaron

hopping mechanisms, respectively.

References

- (1) Scharner, S.; Weppner, W.; SchmidBeurmann, P. Evidence of twophase formation upon lithium insertion into the $\text{Li}_{1.33}\text{Ti}_{1.67}\text{O}_4$ spinel. *J. Electrochem. Soc.* **1999**, *146*, 857–861.
- (2) Perdew, J. P.; Burke, K.; Ernzerhof, M. Generalized gradient approximation made simple. *Phys. Rev. Lett.* **1996**, *77*, 3865–3868.
- (3) J. Clark, S.; Segall, M.; J. Pickard, C.; Hasnip, P.; Probert, M.; Refson, K.; C. Payne, M. First principles methods using CASTEP. *Z. Kristallogr.* **2005**, *220*.
- (4) Grau-Crespo, R.; Hamad, S.; Catlow, C. R. A.; de Leeuw, N. H. Symmetry-adapted configurational modelling of fractional site occupancy in solids. *J. of Phys. Condens. Matter* **2007**, *19*, 256201.
- (5) Monkhorst, H. J.; Pack, J. D. Special points for Brillouin-zone integrations. *Phys. Rev. B* **1976**, *13*, 5188–5192.
- (6) Himmetoglu, B.; Floris, A.; de Gironcoli, S.; Cococcioni, M. "Hubbard-corrected DFT energy functionals: The LDA+U description of correlated systems". *Int. J. Quantum Chem.* **2014**, *114*, 14–49.
- (7) Kick, M.; Reuter, K.; Oberhofer, H. Intricacies of DFT+U, not only in a numeric atom centered orbital framework. *J. Chem. Theor. Comput.* **2019**, *15*, 1705–1718.
- (8) Deskins, N. A.; Rousseau, R.; Dupuis, M. Distribution of Ti^{3+} surface sites in reduced TiO_2 . *J. Phys. Chem. C* **2011**, *115*, 7562–7572.
- (9) Yim, C. M.; Pang, C. L.; Thornton, G. Oxygen vacancy origin of the surface band-gap state of $\text{TiO}_2(110)$. *Phys. Rev. Lett.* **2010**, *104*, 036806.

- (10) Diebold, U. The surface science of titanium dioxide. *Surf. Sci. Rep.* **2003**, *48*, 53–229.
- (11) Nasara, R. N.; Tsai, P.-C.; Lin, S.-K. One-step synthesis of highly oxygen-deficient lithium titanate oxide with conformal amorphous carbon coating as anode material for lithium ion batteries. *Adv. Mater. Interfaces* **2017**, *4*.
- (12) Qiu, J.; Lai, C.; Gray, E.; Li, S.; Qiu, S.; Strounina, E.; Sun, C.; Zhao, H.; Zhang, S. Blue hydrogenated lithium titanate as a high-rate anode material for lithium-ion batteries. *J. Mater. Chem. A* **2014**, *2*, 6353–6358.
- (13) Dorado, B.; Amadon, B.; Freyss, M.; Bertolus, M. DFT + U. *Phys. Rev. B* **2009**, *79*, 235125.
- (14) Allen, J. P.; Watson, G. W. Occupation matrix control of d- and f-electron localisations using DFT + U. *Phys. Chem. Chem. Phys.* **2014**, *16*, 21016–21031.
- (15) Blum, V.; Gehrke, R.; Hanke, F.; Havu, P.; Havu, V.; Ren, X.; Reuter, K.; Scheffler, M. Ab initio molecular simulations with numeric atom-centered orbitals. *Comput. Phys. Commun.* **2009**, *180*, 2175–2196.
- (16) Hubbard, J. Electron correlations in narrow energy bands. *Proc. R. Soc. A* **1963**, *276*, 238–257.
- (17) Anisimov, V.; Zaanen, J.; Andersen, O. K. Band theory and Mott insulators: Hubbard U instead of Stoner I . *Phys. Rev. B* **1991**, *44*, 943–954.
- (18) Dudarev, S. L.; Botton, G. A.; Savrasov, S. Y.; Humphreys, C. J.; Sutton, A. P. Electron-energy-loss spectra and the structural stability of nickel oxide: An LSDA+U study. *Phys. Rev. B* **1998**, *57*, 1505–1509.
- (19) Eschrig, H.; Koepernik, K.; Chaplygin, I. Density functional application to strongly correlated electron systems. *J. Solid State Chem.* **2003**, *176*, 482–495.

- (20) Oberhofer, H.; Blumberger, J. Electronic coupling matrix elements from charge constrained density functional theory calculations using a plane wave basis set. *J. Chem. Phys.* **2010**, *133*, 244105.
- (21) Oberhofer, H.; Reuter, K.; Blumberger, J. Charge Transport in Molecular Materials: An Assessment of Computational Methods. *Chem. Rev.* **2017**, *117*, 10319.